

Odd-Parity Magnetism and Gate-Tunable Edelstein Response in van der Waals Heterostructures

Hanbyul Kim,¹ Chan Bin Bark,¹ Seik Pak,¹ Gibaik Sim,^{1, 2, *} and Moon Jip Park^{1, 3, †}

¹*Department of Physics, Hanyang University, Seoul 04763, Republic of Korea*

²*Department of Physics, University of Melbourne, Grattan Street, Parkville VIC 3010, Australia*

³*Research Institute for Natural Science and High Pressure, Hanyang University, Seoul, 04763, Republic of Korea*

(Dated: February 13, 2026)

Odd-parity magnetism has attracted significant interest for its unconventional spin splitting. However, a concrete microscopic route for its realization remains elusive. In this work, we propose van der Waals heterostructures of stripe antiferromagnets (sAFMs) as an ideal platform for electrically controllable p -wave magnetism. In the sAFM/metal/sAFM structure, the leading RKKY-type exchange interaction is canceled due to the symmetry of the stacking pattern. This exposes a higher-order biquadratic interaction as a dominant contribution that drives a filling-controlled transition from a collinear phase to an orthogonal p -wave configuration. The resulting p -wave phase exhibits a gate-tunable Edelstein response, which originates from magnetic symmetry breaking rather than conventional relativistic spin-momentum locking and remains robust even under substantial spin-orbit coupling. Finally, we propose material candidates for the realization of our theory. Our results establish van der Waals heterostructures as a practical platform for non-relativistic spintronics with electric control of odd-parity spin textures.

Introduction— Momentum-dependent spin splitting is conventionally associated with relativistic spin-orbit coupling (SOC) [1, 2]. However, recent progress in the field of unconventional magnetism has demonstrated that significant spin splitting can arise without relativistic effects [1–7]. A representative class of such materials is altermagnets [8–12]. Despite vanishing net magnetization, the intertwining of magnetic order with crystalline symmetries yields a large exchange-driven spin splitting with even-parity spin texture. The strong spin splitting driven by exchange couplings has positioned such unconventional magnets as a promising platform for a wide range of spintronics applications [13–17].

On the other hand, odd-parity spin textures have been proposed in noncollinear magnets [18–20]. The odd-parity phase can occur when the magnetic order is intertwined with crystalline translations through nonsymmorphic symmetry [21–26]. A prototypical example is a p -wave magnet, whose dispersion exhibits $E_{\uparrow}(\mathbf{k}) = E_{\downarrow}(-\mathbf{k})$, indicating that the spin polarization at \mathbf{k} is opposite to that at $-\mathbf{k}$ [11, 21, 27]. A spin-helix state has been proposed as a candidate realization [28], and bulk materials such as CeNiAsO have been proposed to host the requisite symmetry settings [21, 29, 30]. Nevertheless, an engineerable platform that enables controllable access to such spin textures remains highly desirable.

Here, we propose a magnetic trilayer heterostructure composed of a sAFM/metal/sAFM as a promising platform for p -wave magnetism. The metallic spacer mediates a filling-tunable interlayer exchange that favors an orthogonal configuration of the two stripe order parameters, thereby generating an odd-parity spin texture controllable by electrostatic gating. Recent advances in van der Waals (vdW) magnets [31–38] make this proposal ex-

perimentally realistic. In particular, vdW GdTe_3 retains stripe magnetism down to the monolayer limit [39–41]. Finally, we propose a gate-tunable Edelstein response as a smoking-gun electrical signature of the p -wave phase.

Phenomenological model— We consider the two independent stripe order parameters \mathbf{N}_1 and \mathbf{N}_2 for the top and the bottom layers respectively [See Fig. 1(a)], where the local moment in each layer ($\lambda = 1, 2$) is parameterized as $\mathbf{m}_{\lambda}(\mathbf{r}) = \mathbf{N}_{\lambda} \cos[\mathbf{Q} \cdot (\mathbf{r} - \mathbf{r}_{\lambda})]$, where \mathbf{Q} is the ordering wavevector of the stripe state, \mathbf{r}_{λ} is the layer-dependent registry vector. In the absence of SOC, symmetry considerations allow us to write the free-energy density in a general form as [21, 42, 43],

$$\mathcal{F} = \alpha(T) \sum_{i=1,2} |\mathbf{N}_i|^2 + \beta_1 \left(\sum_{i=1,2} |\mathbf{N}_i|^2 \right)^2 + \beta_2 (\mathbf{N}_1 \cdot \mathbf{N}_2)^2 + J_{\text{eff}} (\mathbf{N}_1 \cdot \mathbf{N}_2) + \dots \quad (1)$$

Here, $\alpha(T)$ governs the intrinsic magnetic stability. The interlayer interaction is characterized by the competition between the electron mediated exchange J_{eff} and the higher-order biquadratic coupling β_1 and β_2 .

Assuming fixed order parameter magnitudes $|\mathbf{N}_1| = |\mathbf{N}_2| \approx N$, the effective free energy depends solely on the relative angle θ . The equilibrium configuration is governed by the competition between the linear and biquadratic exchange couplings,

$$\mathcal{F}(\theta) \approx J_{\text{eff}} N^2 \cos \theta + \beta_2 N^4 \cos^2 \theta. \quad (2)$$

In our model, J_{eff} vanishes due to the geometric cancellation. Microscopically, the effective exchange J_{eff} is generated by the metallic layer via the Ruder-
man–Kittel–Kasuya–Yosida (RKKY)-type contribution

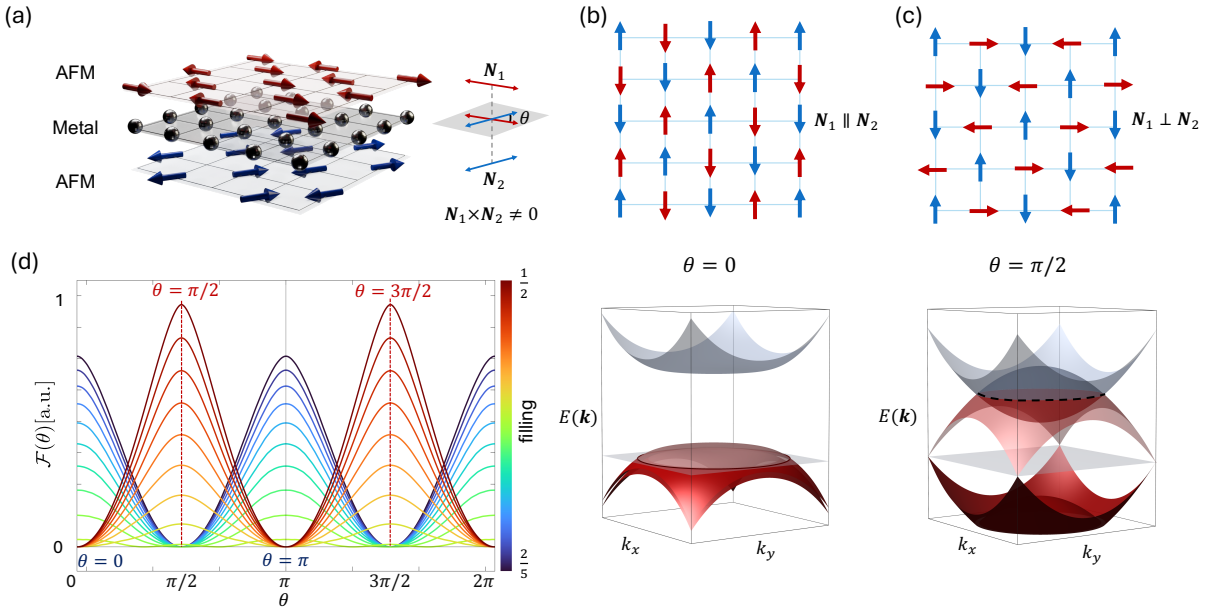


FIG. 1. (a) Schematic of the sAFM/metal/sAFM heterostructure. \mathbf{N}_1 and \mathbf{N}_2 form a relative in-plane angle θ . (b) Band structure for the collinear state ($\theta = 0$), where \mathcal{PT} -symmetry enforces global spin degeneracy. (c) Band structure for the orthogonal state ($\theta = \pi/2$). The breaking of \mathcal{PT} -symmetry lifts the degeneracy, resulting in p -wave band splitting. (d) Relative free energy $\mathcal{F}(\theta)$ as a function of θ for different electronic fillings of the metallic layer. The color gradient indicates filling levels from $n = 1/3$ (blue) to $n = 1/2$ (red). The system undergoes a transition from an orthogonal p -wave phase ($\theta = \pm\pi/2$) at low filling to a collinear phase ($\theta = 0, \pi$) at high filling.

to the free energy, $\Delta\mathcal{F}^{(2)} \sim -\sum_{\mathbf{q}} \mathbf{m}_1(-\mathbf{q}) \chi(\mathbf{q}) \mathbf{m}_2(\mathbf{q})$, where $\chi(\mathbf{q})$ is the static spin-susceptibility tensor of the metal. For the stripe order, only the Fourier components at $\mathbf{q} = \pm\mathbf{Q}$ contribute, giving $J_{\text{eff}} \propto \chi(\mathbf{Q}) \cos(\mathbf{Q} \cdot \boldsymbol{\delta})$ with $\boldsymbol{\delta} = \mathbf{r}_2 - \mathbf{r}_1$ is the registry shift of the two AFM. In our trilayer geometry, the half-translation stacking enforces $\mathbf{Q} \cdot \boldsymbol{\delta} = \pi/2$, and the bilinear exchange vanishes, $J_{\text{eff}} = 0$, independent of microscopic details of $\chi(\mathbf{q})$. More generally, C_{2z} -rotational symmetry maps the sites with opposite magnetic moments onto each other. As a result, the symmetry imposes the cancellation of the linear exchange coupling. (See Sec. III of the Supplemental Material for details.)

In contrast, the biquadratic term β_2 is insensitive to the inversion of the local moments, thus $\beta_2(\mathbf{N}_1 \cdot \mathbf{N}_2)^2$ is non-vanishing leading-order contribution to the free energy. Depending on the sign of β_2 , minimizing the free energy density $f \propto \beta_2 \cos^2 \theta$ presents two distinct scenarios: a negative β_2 would stabilize the collinear alignment [$\theta = 0$, Fig. 1(b)], whereas a positive β_2 favors the orthogonal alignment [$\theta = \pm\pi/2$, Fig. 1(c)], corresponding to the odd-parity magnetism with spin splitting. As we explicitly show in the next section, the change of electron filling alters the sign of β_2 [Fig. 1(d)], where the minimum of $\mathcal{F}(\theta)$ shifts from the collinear configuration near half-filling to the orthogonal configuration at low filling.

Microscopically, the same trend is reflected in the elec-

tronic band structure with θ , as schematically illustrated in Fig. 1(b) and 1(c). For the collinear configuration ($\theta = 0$), a gap opens at half-filling [Fig. 1(b)]. This gap is induced by the staggered Zeeman field associated with the collinear phase analogous to a Slater-type insulating mechanism. The resulting gap formation lowers the electronic energy and therefore favors the collinear state, particularly at half-filling.

Conversely, the orthogonal phase forms a symmetry-protected Dirac nodal line that forbids such global gap opening [Fig. 1(c)]. In this metallic regime, the magnetic instability is driven by kinetic energy minimization. Crucially, the orthogonal configuration lifts the Kramers degeneracy inherent to the collinear phase, inducing a large spin splitting. Away from the half-filling, this splitting pushes the lower spin-branch band. By populating these energetically lowered states, the system can achieve a net reduction in total energy, stabilizing the p -wave state.

Lattice model of odd-parity phases— We implement the proposed magnetic transition by considering the tight-binding Hamiltonian of the metallic layers.

$$\begin{aligned} \hat{H}_{\text{mid}} = & -t \sum_{\langle i,j \rangle, \sigma} (c_{i,\sigma}^\dagger c_{j,\sigma} + \text{h.c.}) - \mu \sum_{i,\sigma} n_{i,\sigma} \\ & + \sum_{i \in A} c_i^\dagger [\mathbf{m}_1(\mathbf{r}_i) \cdot \boldsymbol{\sigma}] c_i + \sum_{j \in B} c_j^\dagger [\mathbf{m}_2(\mathbf{r}_j) \cdot \boldsymbol{\sigma}] c_j, \end{aligned} \quad (3)$$

Here, $c_{i\sigma}^\dagger$ creates an electron with spin σ at site i in

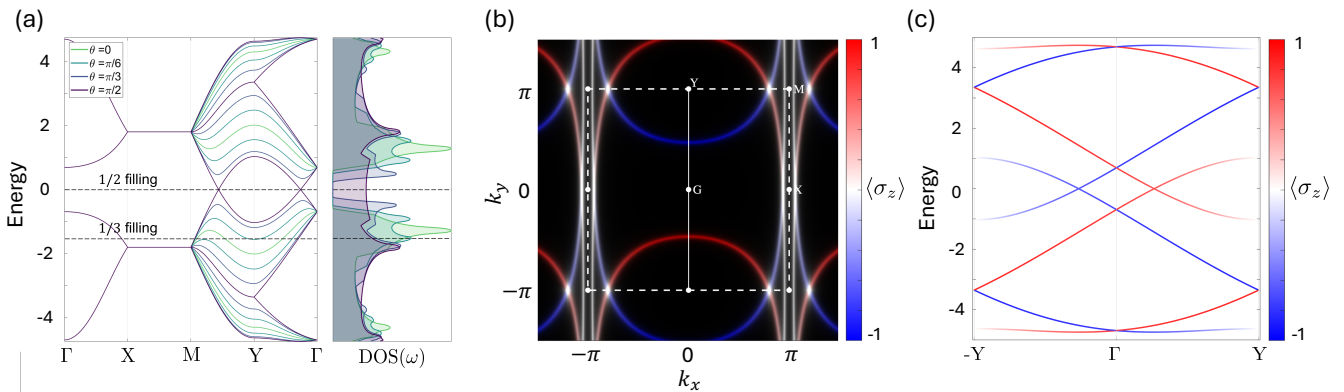


FIG. 2. (a) Evolution of the Bloch bands and density of states (DOS) for different relative angles. The shaded DOS regions highlight the emergence of spectral splitting as θ approaches $\pi/2$. (b) Momentum-space spin polarization map $\langle S_z(\mathbf{k}) \rangle$ at the 1/3-filling. The texture exhibits the characteristic odd-parity symmetry, $\langle S_z(\mathbf{k}) \rangle = -\langle S_z(-\mathbf{k}) \rangle$. (c) Spin-resolved band dispersion along the $Y \rightarrow -Y$ path [white solid line in (b)]. The crossing of opposite spin branches (red and blue) at E_F (dashed line) demonstrates the symmetry-protected p -wave splitting without relativistic SOC.

the middle layer, with t and μ denoting the nearest-neighbor hopping and chemical potential, respectively. The last two terms describe the induced Zeeman potential. Here the top(bottom)-layer magnetization $\mathbf{m}_{t(b)}$ couples exclusively to the A-(B)-sublattice. The stripe spin texture is parametrized as $\mathbf{m}_1(\mathbf{r}) = \mathbf{N}_1 \cos(\mathbf{Q} \cdot \mathbf{r})$ and $\mathbf{m}_2(\mathbf{r}) = \mathbf{N}_2 \cos(\mathbf{Q} \cdot \mathbf{r})$ with $\mathbf{Q} = (\pi, 0)$. Here, although we do not explicitly model the magnetic layers, Eq. (3) represents the effective Hamiltonian derived via a Schrieffer-Wolff (SW) transformation, where integrating out the AFM layers generates the sublattice-selective exchange potentials. (See Sec. II of the Supplemental Material for details of the SW calculation.)

Representative band structures derived from the effective model are shown in Fig. 2(a). At $\theta = 0$, the electronic band retains the global spin degeneracy. This is due to the \mathcal{PT} -symmetry (combining time-reversal with spatial inversion) at the bond center. This symmetry enforces Kramers degeneracy throughout the Brillouin zone (BZ) and opens a global hybridization gap at half-filling. Any deviation from the collinear phase ($\theta \neq 0$) breaks \mathcal{PT} -symmetry, lifting the spin degeneracy. Even for small relative angles, the electronic bands immediately acquire a characteristic p -wave-like odd-parity texture. As the angle approaches the orthogonal limit ($\theta \rightarrow \pi/2$), the spin splitting is maximized.

On the other hand, exactly at $\theta = \pi/2$, we find the formation of the stable Dirac nodal line [Purple line in Fig. 2(b)]. This is due to the nonsymmorphic spin-rotation symmetry, $\mathcal{U}_{\text{ns}} = \{T_{1/2}^x | C_{4z}^S\}$, comprised of a half-translation($T_{1/2}^x$) and 90° spin-rotation(C_{4z}^S) along z -axis. Each band is uniquely labeled by its eigenvalue under the non-symmorphic symmetry \mathcal{U}_{ns} throughout the BZ. The electronic states can be block-diagonalized into distinct sectors labeled by the eigenvalues. In particular,

the bands crossing at the Fermi level belong to different sectors such that their hybridization is forbidden. The symmetry protection ensures that the orthogonal phase remains semimetallic at half-filling, in sharp contrast to the gapped collinear phase.

Upon doping (e.g., $n \sim 1/3$), the energetic hierarchy between the two magnetic configurations reverses. Away from the gap, the instability is driven by the kinetic energy of itinerant carriers. While the collinear phase maintains spin-degenerate bands, the orthogonal phase ($\theta = \pi/2$) breaks \mathcal{PT} -symmetry, inducing a large momentum-dependent spin splitting. This splitting allows electrons to populate the energetically lowered spin-branch. The resulting kinetic energy gain overcomes the magnetic cost, stabilizing the orthogonal p -wave order in the metallic regime. As shown in Fig. 2(b) at $n = 1/3$, the resulting metallic state exhibits an odd-parity spin texture in the out-of-plane direction, $\langle \sigma_z(\mathbf{k}) \rangle = -\langle \sigma_z(-\mathbf{k}) \rangle$ [Fig. 2(b),(c)]. The corresponding dispersion also shows that opposite-spin branches cross without avoided level crossing, demonstrating that the p -wave splitting is symmetry-protected. Further details of the Bloch Hamiltonian and the associated symmetry analysis are provided in Sec. IV of the Supplemental Material.

Perturbative analysis— The effective magnetic free energy can be derived by integrating out the itinerant electronic degrees of freedom. With the linear exchange geometrically suppressed, the leading magnetic interaction arises from fourth-order scattering processes, yielding the biquadratic coefficient β_2 . Analytically, β_2 decomposes

into two competing contributions, $\beta_2 = \beta_2^{\text{FS}} + \beta_2^{\text{sea}}$,

$$\begin{aligned} \beta_2^{\text{FS}} &= \sum_{\mathbf{k}} A_{\mathbf{k}} [\partial_{\epsilon} n_{\text{F}}(\epsilon_{\mathbf{k}} - \mu) + \partial_{\epsilon} n_{\text{F}}(\epsilon_{\mathbf{k}} + \mu)] + (\mathbf{k} \rightarrow \mathbf{k} + \mathbf{Q}), \\ \beta_2^{\text{sea}} &= - \sum_{\mathbf{k}} B_{\mathbf{k}} [n_{\text{F}}(\epsilon_{\mathbf{k}} - \mu) - n_{\text{F}}(-\epsilon_{\mathbf{k}} - \mu)] + (\mathbf{k} \rightarrow \mathbf{k} + \mathbf{Q}), \end{aligned} \quad (4)$$

where n_{F} and $\partial_{\epsilon} n_{\text{F}}$ denotes the Fermi-Dirac distribution function and its derivative respectively. The explicit forms of the prefactors appearing in Eq. (4) are given by $A_{\mathbf{k}} = \frac{\lambda^4 \epsilon_{\mathbf{k}+\mathbf{Q}}^2}{16 \Delta_{\mathbf{k}}^2}$ and $B_{\mathbf{k}} = \frac{\lambda^4 \epsilon_{\mathbf{k}+\mathbf{Q}}^2}{16 \epsilon_{\mathbf{k}} \Delta_{\mathbf{k}}^2} + \frac{\lambda^4 \epsilon_{\mathbf{k}} \epsilon_{\mathbf{k}+\mathbf{Q}}^2}{8 \Delta_{\mathbf{k}}^3}$, with $\Delta_{\mathbf{k}} \equiv \epsilon_{\mathbf{k}}^2 - \epsilon_{\mathbf{k}+\mathbf{Q}}^2$. (See Sec. II of the Supplemental Material for the detailed derivation.) The Fermi-surface term restricts the contribution to the near Fermi surface, whereas the Fermi-sea term integrates over the entire BZ. This decomposition highlights a competition between two distinct instability mechanisms.

From Eq. (4), we find that the Fermi surface and sea term are positive and negative contributions, respectively. Interestingly, this feature is independent of microscopic band dispersions. As shown in Fig. 3(a), the Fermi surface contribution is concentrated at hot spots in the BZ where the nesting condition $\epsilon_{\mathbf{k}} = \epsilon_{\mathbf{k}+\mathbf{Q}}$ is satisfied. This term favors the orthogonal configuration by maximizing exchange-driven band splitting near the Fermi level analogous to the Stoner instability. In stark contrast, the second term represents the Fermi-sea contribution. As shown in Fig. 3(b), this term contributes negatively ($\beta_2 < 0$) and is delocalized across the occupied states. It favors the collinear alignment to open a global hybridization gap, lowering the total energy of the Fermi sea.

Consequently, the magnetic transition is governed by a filling-controlled crossover between these two forces. Fig. 3(c) maps out the resulting phase diagram. Near half-filling, the Fermi-sea contribution dominates due to the gap opening, stabilizing the collinear insulator. However, with doping, the Fermi-surface hot spots dominate the interaction, driving the transition to the orthogonal p -wave metal. This confirms that the odd-parity magnetism is a tunable outcome of Fermi surface engineering.

Edelstein effect.— We propose a gate-tunable Edelstein response as an electrical fingerprint of the p -wave phase. Within the constant relaxation-time approximation, we define the current-induced spin accumulation by a dimensionless Edelstein kernel χ_{ij} in the lattice as

$$\frac{\delta S_i}{\hbar/2} \simeq \chi_{ij} \frac{e E_j a \tau_{\text{sc}}}{\hbar}, \quad (5)$$

where a is the in-plane lattice constant and τ_{sc} is its momentum relaxation time. Here δS_i denotes the nonequilibrium spin polarization per magnetic unit cell, induced by an electric field E_j .

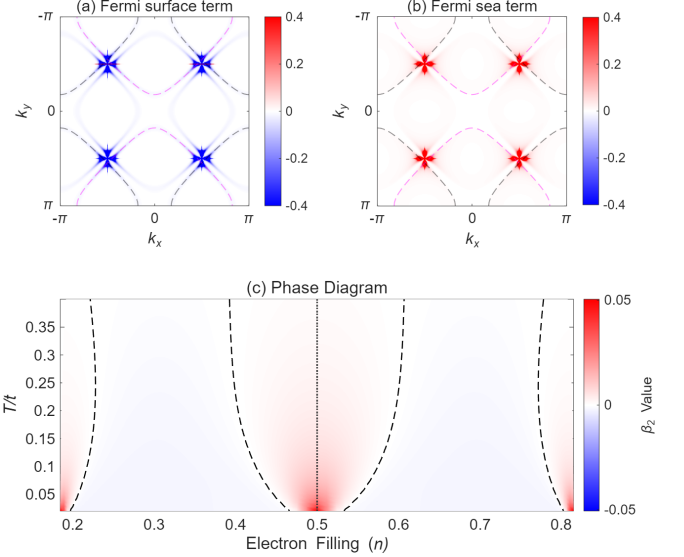


FIG. 3. Microscopic origin of biquadratic exchange and magnetic phase diagram. (a–c) Momentum-resolved distribution of the β_2 integrand components : (a) Fermi surface contribution ($\propto n'_{\text{F}}$), dominating near the chemical potential; (b) Fermi sea contribution ($\propto n_{\text{F}}$), representing energy redistribution of all occupied states (c) Magnetic phase diagram in the filling (n)–temperature (T/t) plane. The orthogonal p -wave phase ($\theta \approx \pi/2$) is stabilized at low fillings by kinetic energy gain, whereas the collinear phase ($\theta = 0, \pi$) is favored near half-filling ($n = 1/2$).

In our system, the out-of-plane spin polarization induced by a y -directed electric field is governed by

$$\chi_{zy} = \sum_n \int_{\text{BZ}} \frac{d^2 k}{(2\pi)^2} \langle \sigma_z \rangle_{n\mathbf{k}} \langle \partial_{k_y} H(\mathbf{k}) \rangle_{n\mathbf{k}} \left(-\partial_{\epsilon} n_{\text{F}}(\epsilon_{n\mathbf{k}} - \mu) \right), \quad (6)$$

where $\langle O \rangle_{n\mathbf{k}} \equiv \langle n\mathbf{k} | O | n\mathbf{k} \rangle$, and $|n\mathbf{k}\rangle$ and $\epsilon_{n\mathbf{k}}$ denote the Bloch eigenstate and eigenvalue, respectively. Here $\partial_{k_y} H(\mathbf{k})$ is evaluated in lattice units so that χ_{zy} is dimensionless; the physical prefactor enters through Eq. (5). In the collinear limit ($\theta = 0$), \mathcal{PT} -symmetry enforces $\chi_{zy} = 0$. Conversely, the orthogonal p -wave phase breaks this symmetry, allowing a finite current-induced spin polarization.

Fig. 4(a) demonstrates the evolution of χ_{zy} as a function of electron filling. The response exhibits a sharp contrast driven by the magnetic phase transition: it vanishes in the collinear regimes but becomes finite within the metallic p -wave windows ($\theta \simeq \pi/2$). This behavior originates from the odd-parity spin splitting at the Fermi surface, as visualized by the momentum-resolved kernel in Fig. 4(c). This gate-tunability is intrinsic to the magnetic texture and robust against relativistic effects, as confirmed by including a Rashba spin-orbit term $H_{\text{soc}} = \lambda_{\text{SO}} (\sin k_x \sigma_y - \sin k_y \sigma_x)$.

Fig. 4(a) shows that strong SOC ($\lambda_{\text{SO}}/t = 0.3$), com-

parable to SOC scales expected in layered Fe-based metals, does not alter the qualitative dependence on filling. Rashba SOC can also generate additional transverse components of the response; indeed, for $\lambda_{SO}/t = 0.1$ we find finite χ_{xy} and χ_{yx} [Fig. 4(b)], but their magnitudes remain subdominant compared to the magnetically generated χ_{zy} in the p -wave regime. This robustness confirms that the observed Edelstein effect is driven by magnetic symmetry breaking, distinguishing it from the conventional mechanism that relies on SOC.

Conclusion.— We have established a microscopic, symmetry-driven route to odd-parity magnetism in a sAFM/metal/sAFM heterostructure. As a concrete vdW-compatible platform, we propose GdTe₃ as a candidate material, where spin-polarized STM identified a low-temperature commensurate sAFM phase below ~ 7 K [39–41]. Using $a \sim 3.1$ Å as a representative in-plane lattice constant (e.g., the lattice constant of the metal layer that is commensurate with GdTe₃ [41]), together with the momentum relaxation time $\tau_{sc} \sim 0.1\text{--}0.3$ ps and an electric field $E_y = 0.1\text{--}1$ kV cm⁻¹, we estimate $\delta S_z \sim 10^{-3}\text{--}10^{-2} (\hbar/2)$ per magnetic unit cell. For a magnetic unit-cell area $A_{cell} \sim 4a^2$, this corresponds to a sheet spin density $\delta S_z/A_{cell} \sim (3 \times 10^{-3}\text{--}3 \times 10^{-2}) (\hbar/2)$ nm⁻², comparable to Edelstein polarizations reported for conventional Rashba interfaces. Since $\delta S_z \propto \tau_{sc}$, optimizing the spacer quality and interfaces can further enhance the signal, making the effect readily measurable in clean heterostructures.

Besides vdW materials, the same design principle applies to epitaxial thin films of layered sAFM, including the iron pnictide family (AFe₂As₂ with A = Ca, Sr, Ba; RFeAsO with R = rare earth; and NaFeAs), which host robust stripe order on nearly square Fe lattices[44–51]. Among available platforms, vdW assembly is particularly appealing: exfoliation and dry-transfer stacking enable deterministic control of twist and registry.

ACKNOWLEDGMENTS

We thank Changmin Lee for fruitful discussions. This work was supported by the National Research Foundation of Korea (NRF) grant funded by the Korea government (MSIT) (Grants No. RS-2025-16070482, RS-2025-25446099, RS-2025-03392969, RS-2025-25464760, RS-2025-25431194, RS-2025-25433233 for H.U.). This work was also supported by BK21 FOUR (Fostering Outstanding Universities for Research) program through the National Research Foundation (NRF) funded by the Ministry of Education of Korea.

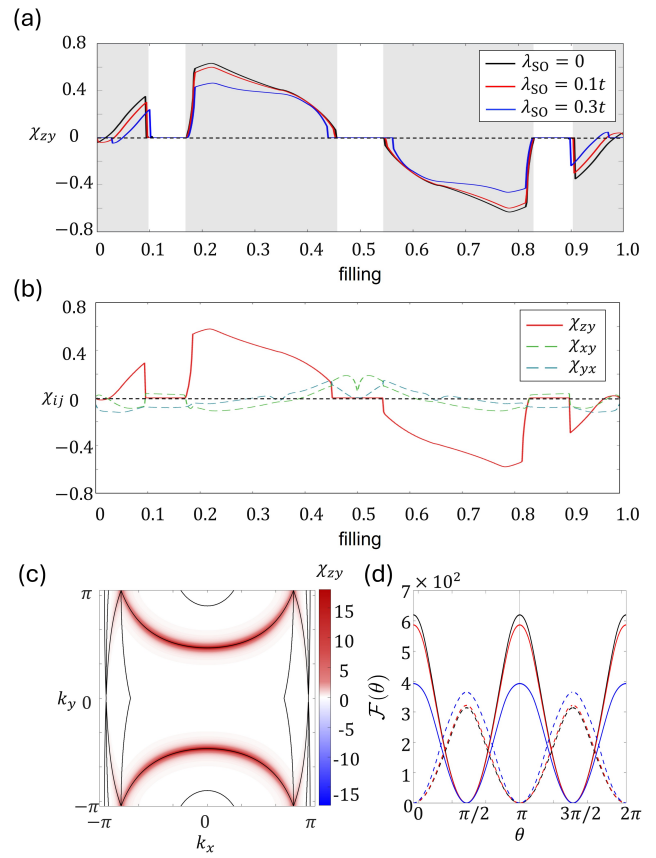


FIG. 4. (a) Edelstein kernel χ_{zy} as a function of electronic filling for different SOC strengths. The shaded regions indicate the p -wave phase ($\theta \approx \pi/2$) where the response is significant. (b) Filling dependence of representative tensor components χ_{ij} in the presence of Rashba SOC ($\lambda_{SO}/t = 0.1$), showing that transverse components (e.g., χ_{xy} and χ_{yx}) remain subdominant to χ_{zy} in the p -wave regime. (c) Momentum-resolved kernel of the response, showing the odd-parity distribution over the Fermi surface (black lines). (d) Relative total energy $\mathcal{F}(\theta)$ for representative fillings of $1/2$ (collinear stable) and $1/3$ (orthogonal stable).

[†] moonjippark@hanyang.ac.kr

- [1] Y. A. Bychkov and E. I. Rashba, *Journal of Physics C: Solid State Physics* **17**, 6039 (1984).
- [2] G. Bihlmayer, P. Noël, D. V. Vyalikh, E. V. Chulkov, and A. Manchon, *Nature Reviews Physics* **4**, 642–659 (2022).
- [3] M. Naka, S. Hayami, H. Kusunose, Y. Yanase, and Y. Motome, *Nature Communications* **10**, 4305 (2019).
- [4] L. Šmejkal, R. González-Hernández, T. Jungwirth, and J. Sinova, *Science Advances* **6**, eaaz8809 (2020).
- [5] S. Hayami, Y. Yanagi, and H. Kusunose, *Journal of the Physical Society of Japan* **88**, 123702 (2019).
- [6] L.-D. Yuan, Z. Wang, J.-W. Luo, E. I. Rashba, and A. Zunger, *Physical Review B* **102**, 014422 (2020).
- [7] L. Šmejkal, J. Sinova, and T. Jungwirth, *Physical Review X* **12**, 031042 (2022).
- [8] I. I. Mazin, *Physical Review X* **12**, 040002 (2022).
- [9] J. Krempaský, L. Šmejkal, S. W. D’Souza, *et al.*, *Nature* **626**, 517 (2024).

* gibaik.sim@unimelb.edu.au

[10] Z. Feng, X. Zhou, L. Šmejkal, *et al.*, *Nature Electronics* **5**, 735 (2022).

[11] R. Gonzalez-Hernandez, L. Šmejkal, K. Výborný, *et al.*, *Physical Review Letters* **126**, 127701 (2021).

[12] J. Betancourt, J. Zubáč, R. Gonzalez-Hernandez, *et al.*, *Physical Review Letters* **130**, 036702 (2023).

[13] A. Bose, N. J. Schreiber, R. Jain, *et al.*, *Nature Electronics* **5**, 267 (2022).

[14] H. Bai, L. Han, X. Y. Feng, *et al.*, *Physical Review Letters* **128**, 197202 (2022).

[15] S. Karube, T. N. Tanaka, D. Sugawara, *et al.*, *Physical Review Letters* **129**, 137201 (2022).

[16] L. Šmejkal, J. Sinova, and T. Jungwirth, *Nature Reviews Materials* **7**, 482 (2022).

[17] D.-F. Shao, S.-H. Zhang, M. Li, C.-B. Eom, and E. Y. Tsymbal, *Nature Communications* **12**, 7061 (2021).

[18] L. Šmejkal, J. Sinova, and T. Jungwirth, *Nature Reviews Materials* **7**, 482 (2022).

[19] S. Hayami, Y. Yanagi, and H. Kusunose, *Journal of the Physical Society of Japan* **88**, 123702 (2019).

[20] L.-D. Yuan, Z. Wang, J.-W. Luo, E. I. Rashba, and A. Zunger, *Physical Review B* **102**, 014422 (2020).

[21] Y. Yu, M. B. Lyngby, T. Shishidou, M. Roig, A. Kreisel, M. Weinert, B. M. Andersen, and D. F. Agterberg, *Physical Review Letters* **135**, 046701 (2025).

[22] X. Zhang, Q. Liu, J.-W. Luo, A. J. Freeman, and A. Zunger, *Nature Physics* **10**, 387 (2014).

[23] L. L. Tao, *Phys. Rev. B* **110**, L121125 (2024).

[24] H. Watanabe and Y. Yanase, *Journal of Physics: Condensed Matter* **36**, 373001 (2024).

[25] C. Lee and P. M. R. Brydon, *Physical Review Letters* **135**, 116701 (2025).

[26] C. Lee, N. A. Hackner, and P. M. R. Brydon, arXiv preprint arXiv:2508.06713 [10.48550/arXiv.2508.06713](https://arxiv.org/abs/2508.06713) (2025), [arXiv:2508.06713 \[cond-mat.mes-hall\]](https://arxiv.org/abs/2508.06713).

[27] L. Han, X. Fu, R. Peng, X. Cheng, J. Dai, L. Liu, Y. Li, Y. Zhang, W. Zhu, H. Bai, Y. Zhou, S. Liang, C. Chen, Q. Wang, X. Chen, L. Yang, Y. Zhang, C. Song, J. Liu, and F. Pan, *Science Advances* **10**, eadn0479 (2024).

[28] Q. Song, S. Stavrić, P. Barone, A. Droghetti, D. S. Antonenko, J. W. F. Venderbos, C. A. Occhialini, B. Ilyas, E. Ergeçen, N. Gedik, S.-W. Cheong, R. M. Fernandes, S. Picozzi, and R. Comin, *Nature* **642**, 64 (2025).

[29] A. Chakraborty, A. B. Hellenes, R. Jaeschke-Ubiergo, T. Jungwirth, L. Šmejkal, and J. Sinova, arXiv preprint (2024), [2411.16378](https://arxiv.org/abs/2411.16378).

[30] M. Hu, O. Janson, C. Felser, P. McClarty, J. v. d. Brink, and M. G. Vergniory, arXiv preprint (2024), [2410.17993](https://arxiv.org/abs/2410.17993).

[31] Y. Deng, Y. Yu, Y. Song, J. Zhang, N. Z. Wang, Z. Sun, Y. Yi, Y. Wu, S. Wu, J. Zhu, J. Wang, X. H. Chen, and Y. Zhang, *Nature* **563**, 94 (2018).

[32] K. S. Burch, D. Mandrus, and J.-G. Park, *Nature* **563**, 47 (2018).

[33] M. Gibertini, M. Koperski, A. F. Morpurgo, and K. S. Novoselov, *Nature Nanotechnology* **14**, 408 (2019).

[34] H. Chu, C. J. Roh, J. O. Island, C. Li, S. Lee, J. Chen, J.-G. Park, E. Rotenberg, S.-K. Lee, and D. Hsieh, *Physical Review Letters* **124**, 027601 (2020).

[35] M. Steiner, *Antiferromagnetism and electronic states in 2D transition metal phosphorus trisulphides*, *Master's thesis*, Johannes Kepler University Linz (2020).

[36] Z. Ni, H. Zhang, D. Hopper, A. Haglund, N. Huang, D. Jariwala, L. C. Bassett, D. Mandrus, E. J. Mele, C. L. Kane, and L. Wu, *Physical Review Letters* **127**, 187201 (2021).

[37] K. Kim, S. Y. Lim, J. Lee, S. Lee, T. Y. Kim, K. Park, G. S. Jeon, C. Park, J. Park, and H. Cheong, *2D Materials* **6**, 041001 (2019).

[38] T. Y. Kim and C.-H. Park, *Nano Letters* **21**, 10114 (2021).

[39] A. Raghavan, M. Romanelli, J. May-Mann, A. Aishwarya, L. Aggarwal, A. G. Singh, M. D. Bachmann, L. M. Schoop, E. Fradkin, I. R. Fisher, and V. Madhavan, *npj Quantum Materials* **9**, [10.1038/s41535-024-00660-4](https://doi.org/10.1038/s41535-024-00660-4) (2024).

[40] Z. Xu, S.-H. Ji, L. Tang, J. Wu, N. Li, X. Cai, and X. Chen, *Chinese Physics Letters* **38**, 077102 (2021).

[41] S. Lei, J. Lin, Y. Jia, M. Gray, A. Topp, G. Farahi, S. Klemenz, T. Gao, F. Rodolakis, J. L. McChesney, C. R. Ast, A. Yazdani, K. S. Burch, S. Wu, N. P. Ong, and L. M. Schoop, *Science Advances* **6**, [10.1126/sci-adv.aaay6407](https://doi.org/10.1126/sci-adv.aaay6407) (2020).

[42] I. P. Ivanov, *Physical Review E* **79**, 021116 (2009).

[43] H. Watanabe and Y. Yanase, *Phys. Rev. B* **98**, 245129 (2018).

[44] A. Jesche, N. Caroca-Canales, H. Rosner, H. Borrmann, A. Ormeci, D. Kasinathan, H. H. Klauss, H. Luetkens, R. Khasanov, A. Amato, A. Hoser, K. Kaneko, C. Krellner, and C. Geibel, *Phys. Rev. B* **78**, 180504 (2008).

[45] Q. Huang, Y. Qiu, W. Bao, M. A. Green, J. W. Lynn, Y. C. Gasparovic, T. Wu, G. Wu, and X. H. Chen, *Phys. Rev. Lett.* **101**, 257003 (2008).

[46] A. I. Goldman, D. N. Argyriou, B. Ouladdiaf, T. Chatterji, A. Kreyssig, S. Nandi, N. Ni, S. L. Bud'ko, P. C. Canfield, and R. J. McQueeney, *Phys. Rev. B* **78**, 100506 (2008).

[47] C. de la Cruz, Q. Huang, J. W. Lynn, J. Li, W. R. II, J. L. Zarestky, H. A. Mook, G. F. Chen, J. L. Luo, N. L. Wang, and P. Dai, *Nature* **453**, 899–902 (2008).

[48] J. Zhao, Q. Huang, C. de la Cruz, S. Li, J. W. Lynn, Y. Chen, M. A. Green, G. F. Chen, G. Li, Z. Li, J. L. Luo, N. L. Wang, and P. Dai, *Nature Materials* **7**, 953–959 (2008).

[49] J. Zhao, Q. Huang, C. de la Cruz, J. W. Lynn, M. D. Lumsden, Z. A. Ren, J. Yang, X. Shen, X. Dong, Z. Zhao, and P. Dai, *Phys. Rev. B* **78**, 132504 (2008).

[50] Y. Chen, J. W. Lynn, J. Li, G. Li, G. F. Chen, J. L. Luo, N. L. Wang, P. Dai, C. de la Cruz, and H. A. Mook, *Phys. Rev. B* **78**, 064515 (2008).

[51] P. Dai, *Rev. Mod. Phys.* **87**, 855 (2015).

[52] S. Bravyi, D. P. DiVincenzo, and D. Loss, *Annals of Physics* **326**, 2793 (2011).

CONTENTS

I. Microscopic Hamiltonian	i
II. Derivation of Free energy for Spin Model	ii
A. Schrieffer-Wolff Transformation	ii
B. Path Integral Formulation	iii
C. Integration over electronic degrees of freedom	iii
D. Perturbative Expansion	iv
1. Analytical calculation of coefficient β_2	v
III. Geometric cancellation of the bilinear exchange J_{eff}	v
IV. Symmetry of the tight-binding model	vi
A. Symmetry constraint on spin polarization of odd-parity magnetism	vii
B. Kramers degeneracy on Γ -X	ix
C. Kramers degeneracy on X -M	ix
D. Non-symmorphic symmetry \mathcal{U}_{ns} at $\theta = \pi/2$	ix
E. \mathcal{PT} -symmetry at $\theta = 0$	x

I. MICROSCOPIC HAMILTONIAN

We consider a van der Waals trilayer system consisting of two stripe antiferromagnetic (AFM) insulators (top and bottom) and a central metallic layer. The system is modeled on a two-dimensional square lattice with coordinates $\mathbf{r}_i = (x_i, y_i)$ and lattice constant $a = 1$. The total Hamiltonian is $\hat{H}_{\text{tot}} = \hat{H}_{\text{mid}} + \hat{H}_{\text{top}} + \hat{H}_{\text{bot}} + \hat{V}_{\text{int}}$.

$$\hat{H}_{\text{mid}} = -t_m \sum_{\langle i,j \rangle, \sigma} (c_{i,\sigma}^\dagger c_{j,\sigma} + \text{h.c.}) - \mu \sum_{i,\sigma} n_{i,\sigma}, \quad (\text{S1})$$

$$\hat{H}_{\text{top}} = -t_{\text{AFM}} \sum_{\langle i,j \rangle \in \text{T}, \sigma} d_{i,\sigma,\text{T}}^\dagger d_{j,\sigma,\text{T}} + J \sum_{i \in \text{T}} d_{i,\text{T}}^\dagger [\mathbf{m}_\text{T}(\mathbf{r}_i) \cdot \boldsymbol{\sigma}] d_{i,\text{T}}, \quad (\text{S2})$$

$$\hat{H}_{\text{bot}} = -t_{\text{AFM}} \sum_{\langle i,j \rangle \in \text{B}, \sigma} d_{i,\sigma,\text{B}}^\dagger d_{j,\sigma,\text{B}} + J \sum_{i \in \text{B}} d_{i,\text{B}}^\dagger [\mathbf{m}_\text{B}(\mathbf{r}_i) \cdot \boldsymbol{\sigma}] d_{i,\text{B}}. \quad (\text{S3})$$

Here, the middle layer is described by a standard tight-binding model on a square lattice. $c_{i,\sigma}^\dagger$ creates an electron with spin σ at site i in the middle layer, t_m is the nearest-neighbor hopping amplitude within the middle layer, and μ represents the chemical potential. The operator $n_{i,\sigma} = c_{i,\sigma}^\dagger c_{i,\sigma}$ is the particle number operator. The top and bottom layers are modeled as stripe antiferromagnets. $d_{i,\lambda}^\dagger = (d_{i,\uparrow,\lambda}^\dagger, d_{i,\downarrow,\lambda}^\dagger)$ is the spinor operator for layer $\lambda \in \{\text{T}, \text{B}\}$. t_{AFM} denotes the intralayer hopping amplitude within the AFM layers.

The magnetic configuration is characterized by the vector order parameters \mathbf{N}_1 and \mathbf{N}_2 for the top and bottom layers, respectively. The local magnetic texture at each site $\mathbf{r}_i = (x_i, y_i)$ is determined by the stripe wavevector $\mathbf{Q} = (\pi, 0)$ as follows:

$$\mathbf{m}_\text{T}(\mathbf{r}_i) = \mathbf{N}_1 \cos(\mathbf{Q} \cdot \mathbf{r}_i), \quad \mathbf{m}_\text{B}(\mathbf{r}_i) = \mathbf{N}_2 \cos(\mathbf{Q} \cdot \mathbf{r}_i), \quad (\text{S4})$$

The relative shift of stacking between the top and bottom AFM layers is denoted by $\delta = \hat{x}/2$. The vector $\boldsymbol{\sigma} = (\sigma_x, \sigma_y, \sigma_z)$ is the vector of Pauli matrices acting on the electron spins.

Vertical tunneling with amplitude t_\perp describes the hybridization between the layers. We assume the top layer couples selectively to the A-sublattice of the middle layer, while the bottom layer couples to the B-sublattice as

$$\hat{V}_{\text{int}} = -t_\perp \sum_{i \in \text{A}} (d_{i,\text{T}}^\dagger c_i + \text{h.c.}) - t_\perp \sum_{j \in \text{B}} (d_{j,\text{B}}^\dagger c_j + \text{h.c.}), \quad (\text{S5})$$

where t_\perp is the vertical tunneling amplitude.

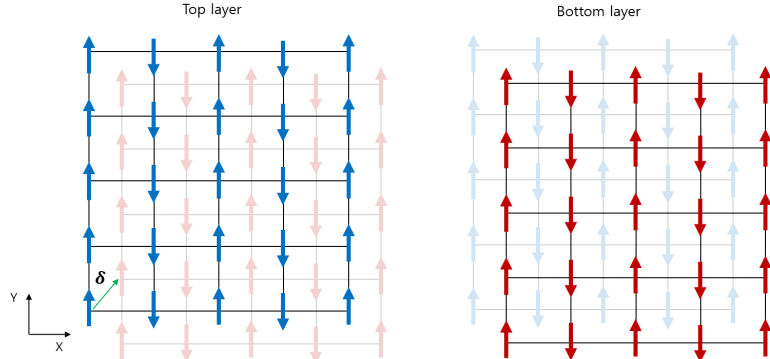


FIG. S1. Stripe antiferromagnetic order in top and bottom layers for visual clarification.

II. DERIVATION OF FREE ENERGY FOR SPIN MODEL

In the main text in Eq. (1), the phenomenological Landau free energy of the trilayer system is written as,

$$\mathcal{F}_{\text{spin}} [\mathbf{N}_1, \mathbf{N}_2] = \alpha \sum_{i=1,2} |\mathbf{N}_i|^2 + \beta_1 \left(\sum_{i=1,2} |\mathbf{N}_i|^2 \right)^2 + \beta_2 (\mathbf{N}_1 \cdot \mathbf{N}_2)^2 + J_{\text{eff}} (\mathbf{N}_1 \cdot \mathbf{N}_2) + \dots \quad (\text{S6})$$

Here, we provide a microscopic derivation of this free energy, starting from the trilayer Hamiltonian in Eq. (S3) and deriving the low-energy effective model in Eq. (S8).

A. Schrieffer-Wolff Transformation

Assuming that the interlayer hopping t_{\perp} is small, we treat the interlayer hybridization \hat{V}_{int} as a perturbation. To derive the effective Hamiltonian for the low-energy subspace (central metallic layer), we employ the Schrieffer-Wolff transformation[52]. We define the projection operators P onto the low-energy subspace of middle layer states, and $Q = 1 - P$ as the complementary space. The effective Hamiltonian in the leading order is given by:

$$\hat{H}_{\text{eff}} = P \hat{V}_{\text{int}} Q \frac{1}{E - \hat{H}_0} Q \hat{V}_{\text{int}} P. \quad (\text{S7})$$

In the static limit ($E \approx 0$), the effective interactions on A and B sublattices generate induced Zeeman fields. Summing over all sites, the low-energy effective Hamiltonian for the middle layer becomes a square lattice model with sublattice-dependent exchange fields as,

$$\hat{H}_{\text{eff}} = -t_m \sum_{\langle i,j \rangle, \sigma} (c_{i,\sigma}^\dagger c_{j,\sigma} + \text{h.c.}) - \mu \sum_{i,\sigma} n_{i,\sigma} + \sum_{i \in A} c_i^\dagger [\mathbf{h}_A(\mathbf{r}_i) \cdot \boldsymbol{\sigma}] c_i + \sum_{j \in B} c_j^\dagger [\mathbf{h}_B(\mathbf{r}_j) \cdot \boldsymbol{\sigma}] c_j. \quad (\text{S8})$$

where the effective Zeeman fields are given as,

$$\mathbf{h}_A(\mathbf{r}_i) \equiv -\frac{t_{\perp}^2}{J |\mathbf{m}_T(\mathbf{r}_i)|^2} \mathbf{m}_T(\mathbf{r}_i), \quad \mathbf{h}_B(\mathbf{r}_j) \equiv -\frac{t_{\perp}^2}{J |\mathbf{m}_B(\mathbf{r}_j)|^2} \mathbf{m}_B(\mathbf{r}_j). \quad (\text{S9})$$

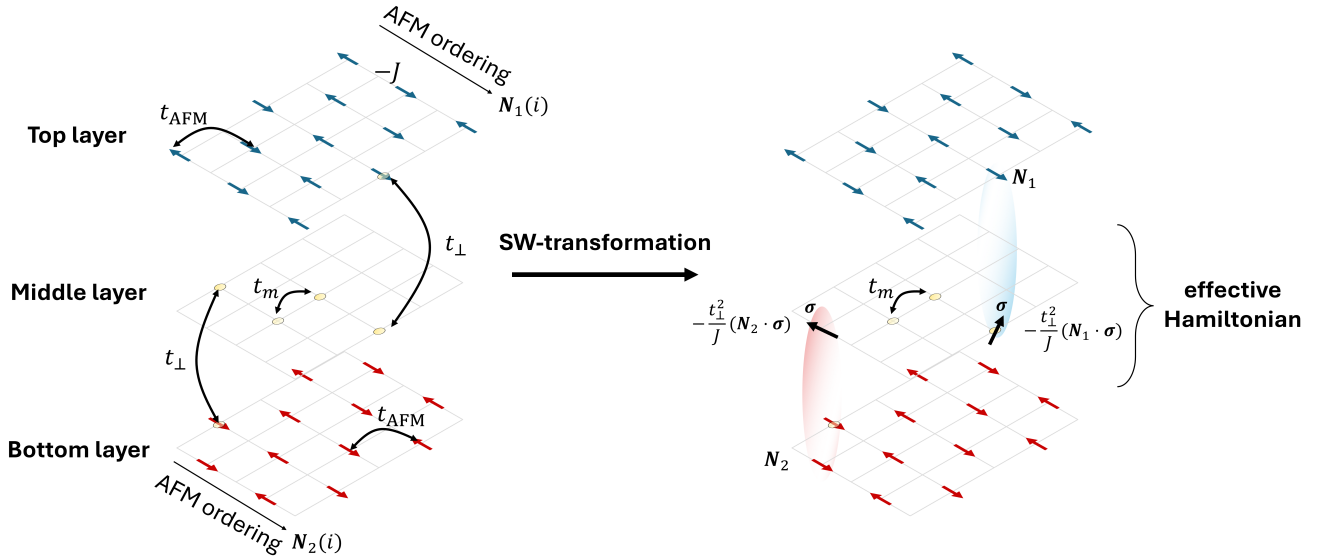


FIG. S2. Schematic illustration of the microscopic Hamiltonian and the effective Hamiltonian after Schrieffer-Wolff transformation

B. Path Integral Formulation

To microscopically derive the coefficients of the free energy in Eq. (S6), we employ the path-integral formalism and integrate out the itinerant electrons of the middle layer in Eq. (S8). The full partition function is written as,

$$\mathcal{Z}_{\text{full}} = \int \mathcal{D}\mathbf{N}_1 \mathcal{D}\mathbf{N}_2 \mathcal{D}c^\dagger \mathcal{D}c e^{-S_{\text{tot}}[c, c^\dagger; \mathbf{N}_1, \mathbf{N}_2]} = \int \mathcal{D}\mathbf{N}_1 \mathcal{D}\mathbf{N}_2 e^{-\beta \mathcal{F}_{\text{spin}}[\mathbf{N}_1, \mathbf{N}_2]}, \quad (\text{S10})$$

The total action is given as, $S_{\text{tot}} = S_{\text{el}}[c, c^\dagger] + S_{\text{int}}[c, c^\dagger; \mathbf{N}_1, \mathbf{N}_2] + S_{\text{loc}}[\mathbf{N}_1, \mathbf{N}_2]$. $\mathcal{F}_{\text{spin}}$ is the effective free energy in Eq. (S6).

$$S_{\text{el}} = \int_0^\beta d\tau \sum_{\mathbf{k}} c_{\mathbf{k}}^\dagger(\tau) (\partial_\tau + \varepsilon_{\mathbf{k}} - \mu) c_{\mathbf{k}}(\tau), \quad (\text{S11})$$

$$S_{\text{int}} = \int_0^\beta d\tau \left[\sum_{i \in A} c_i^\dagger(\tau) (\mathbf{h}_A(\mathbf{r}_i) \cdot \boldsymbol{\sigma}) c_i(\tau) + \sum_{j \in B} c_j^\dagger(\tau) (\mathbf{h}_B(\mathbf{r}_j) \cdot \boldsymbol{\sigma}) c_j(\tau) \right]. \quad (\text{S12})$$

Here S_{el} is the free-electron action of the middle layer with the dispersion $\varepsilon_{\mathbf{k}} = -2t_m(\cos k_x + \cos k_y)$. S_{int} encodes the induced sublattice-dependent exchange fields obtained from Eq. (S8). Finally, $S_{\text{loc}}[\mathbf{N}_1, \mathbf{N}_2]$ denotes the intrinsic magnetic free-energy of forming the stripe-AFM order. Its explicit form is not required for extracting the electron-mediated contributions to the Landau expansion and will be left unspecified.

C. Integration over electronic degrees of freedom

We first rewrite the electron fields in the two-sublattice basis $c_{\mathbf{k}} = (c_{\mathbf{k}A}, c_{\mathbf{k}B})^T$, where each component is a two-component spinor in spin space. Pauli matrices $\tau_{x,y,z}$ act in the sublattice (A/B) space, while $\boldsymbol{\sigma}$ acts in the spin space. Fourier transforming $c_i(\tau) = \frac{1}{\sqrt{\beta}} \sum_n e^{-i\omega_n \tau} c_i(i\omega_n)$ with the Matsubara frequency $\omega_n = (2n+1)\pi/\beta$, the free-electron action in Eq. (S11) and Eq.(S12) becomes

$$S_{\text{el}} = \sum_n \sum_{\mathbf{k}} c_{\mathbf{k}}^\dagger(i\omega_n) [(-i\omega_n - \mu) + \varepsilon_{\mathbf{k}} \tau_x] c_{\mathbf{k}}(i\omega_n), \quad (\text{S13})$$

$$S_{\text{int}} = \frac{\lambda}{2} \sum_n \sum_{\mathbf{k}} [c_{\mathbf{k}+\mathbf{Q}}^\dagger(i\omega_n) V_{\mathbf{Q}} c_{\mathbf{k}}(i\omega_n) + c_{\mathbf{k}}^\dagger(i\omega_n) V_{\mathbf{Q}}^\dagger c_{\mathbf{k}+\mathbf{Q}}(i\omega_n)]. \quad (\text{S14})$$

Here, the bare Green function is given as $G_0^{-1}(\mathbf{k}, i\omega_n) = (-i\omega_n - \mu) + \varepsilon_{\mathbf{k}} \tau_x$. The coupling coefficient is given by, $\lambda = -\frac{t_\perp^2}{J|\mathbf{N}|^2}$ assuming $|\mathbf{N}_1| = |\mathbf{N}_2| \equiv N$. The matrix elements for the Zeeman term are explicitly given as,

$$V_{\mathbf{Q}} = P_A \otimes (\mathbf{N}_1 \cdot \boldsymbol{\sigma}) + P_B \otimes (\mathbf{N}_2 \cdot \boldsymbol{\sigma}), \quad P_A = \begin{pmatrix} 1 & 0 \\ 0 & 0 \end{pmatrix}, \quad P_B = \begin{pmatrix} 0 & 0 \\ 0 & 1 \end{pmatrix}. \quad (\text{S15})$$

where $P_{A(B)}$ are the sublattice projector.

To account for the scattering between \mathbf{k} and $\mathbf{k} + \mathbf{Q}$, we define the enlarged spinor $\Psi_{\mathbf{k}}(i\omega_n) = [c_{\mathbf{k}}(i\omega_n), c_{\mathbf{k}+\mathbf{Q}}(i\omega_n)]^T$. Then, we can rewrite this as $S_{\text{el}} + S_{\text{int}} = \sum_{n,\mathbf{k}} \Psi_{\mathbf{k}}^\dagger \mathcal{G}^{-1}(\mathbf{k}, i\omega_n) \Psi_{\mathbf{k}}$ with

$$\mathcal{G}^{-1}(\mathbf{k}, i\omega_n) = \begin{pmatrix} G_0^{-1}(\mathbf{k}, i\omega_n) & 0 \\ 0 & G_0^{-1}(\mathbf{k} + \mathbf{Q}, i\omega_n) \end{pmatrix} + \frac{\lambda}{2} \begin{pmatrix} 0 & V_{\mathbf{Q}} \\ V_{\mathbf{Q}}^\dagger & 0 \end{pmatrix}. \quad (\text{S16})$$

Integrating out fermionic part in Eq. (S10) using the identity $(\int \mathcal{D}c^\dagger \mathcal{D}c e^{-\sum c^\dagger M c} = \det M)$ yields

$$\begin{aligned} \int \mathcal{D}c^\dagger \mathcal{D}c e^{-(S_{\text{el}} + S_{\text{int}})} &= \prod_n \prod_{\mathbf{k}} \det [\mathcal{G}^{-1}(\mathbf{k}, i\omega_n)] \\ &= \prod_n \prod_{\mathbf{k}} \det [G_0^{-1}(\mathbf{k}, i\omega_n)] \det [G_0^{-1}(\mathbf{k} + \mathbf{Q}, i\omega_n)] \det [I - \frac{\lambda^2}{4} G_0(\mathbf{k}, i\omega_n) V_{\mathbf{Q}} G_0(\mathbf{k} + \mathbf{Q}, i\omega_n) V_{\mathbf{Q}}^\dagger]. \end{aligned} \quad (\text{S17})$$

The first two determinants reproduce the free electron contribution $\mathcal{Z}_0 = e^{-\beta F_0}$, while the third determinant encodes the electron-mediated magnetic interactions.

Finally the effective free energy of spins, $\mathcal{F}_{\text{spin}}$ is obtained by using the operator identity $\ln(\det \hat{A}) = \text{Tr}(\ln \hat{A})$,

$$\mathcal{F}_{\text{spin}}[\mathbf{N}_1, \mathbf{N}_2] = F_{\text{loc}} - \frac{1}{\beta} \sum_n \sum_k \text{Tr} \ln \left[I - \frac{\lambda^2}{4} G_0(\mathbf{k}, i\omega_n) V_{\mathbf{Q}} G_0(\mathbf{k} + \mathbf{Q}, i\omega_n) V_{\mathbf{Q}}^\dagger \right]. \quad (\text{S18})$$

Here, the trace runs over sublattice and spin indices. This exact expression serves as the starting point for the perturbative expansion.

D. Perturbative Expansion

Assuming the induced exchange coupling is small compared to the Fermi energy ($|\lambda| \ll E_F$), we can expand the logarithmic term in powers of the Zeeman potential. Using the Taylor expansion $\ln(1 - x) = -x - \frac{x^2}{2} + \dots$, the correction to the free energy is given as,

$$\Delta \mathcal{F} = \frac{1}{\beta} \sum_{n, \mathbf{k}} \sum_{m=1}^{\infty} \frac{1}{m} \text{Tr} \left[\left(\frac{\lambda^2}{4} G_0(\mathbf{k}) V_{\mathbf{Q}} G_0(\mathbf{k} + \mathbf{Q}) V_{\mathbf{Q}}^\dagger \right)^m \right]. \quad (\text{S19})$$

The first-order expansion gives the bilinear magnetic interaction, which corresponds to the RKKY mechanism.

$$\mathcal{F}^{(1)} = \frac{1}{\beta} \sum_n \sum_k \text{Tr} \left[\frac{\lambda^2}{4} G_0(\mathbf{k}) V_{\mathbf{Q}} G_0(\mathbf{k} + \mathbf{Q}) V_{\mathbf{Q}}^\dagger \right] \quad (\text{S20})$$

Similarly, the second-order term generates higher-order magnetic interactions, including the biquadratic coupling $(\mathbf{N}_1 \cdot \mathbf{N}_2)^2$.

$$\mathcal{F}^{(2)} = \frac{1}{2\beta} \sum_n \sum_k \text{Tr} \left[\left(\frac{\lambda^2}{4} G_0(\mathbf{k}) V_{\mathbf{Q}} G_0(\mathbf{k} + \mathbf{Q}) V_{\mathbf{Q}}^\dagger \right)^2 \right]. \quad (\text{S21})$$

Each coefficient of the Landau free energy in Eq. (S6) is derived explicitly as follows.

- J_{eff} : Using the spin trace identity, $\text{Tr}_{\sigma}[(\mathbf{N}_1 \cdot \boldsymbol{\sigma})(\mathbf{N}_2 \cdot \boldsymbol{\sigma})] = 2(\mathbf{N}_1 \cdot \mathbf{N}_2)$, we derive:

$$J_{\text{eff}} = \frac{\lambda^2}{\beta} \sum_n \sum_k \text{Tr} \left[G_0(\mathbf{k}, i\omega_n) P_A G_0(\mathbf{k} + \mathbf{Q}, i\omega_n) P_B \right], \quad (\text{S22})$$

- β_2 : Using the spin trace identity, we derive:

$$\text{Tr}_{\sigma}[(\mathbf{N}_1 \cdot \boldsymbol{\sigma})(\mathbf{N}_2 \cdot \boldsymbol{\sigma})(\mathbf{N}_1 \cdot \boldsymbol{\sigma})(\mathbf{N}_2 \cdot \boldsymbol{\sigma})] = 4(\mathbf{N}_1 \cdot \mathbf{N}_2)^2 - 2|\mathbf{N}_1|^2|\mathbf{N}_2|^2, \quad (\text{S23})$$

we obtain:

$$\beta_2 = \frac{\lambda^4}{4\beta} \sum_n \sum_k \text{Tr} \left[G_0(\mathbf{k}) P_A G_0(\mathbf{k} + \mathbf{Q}) P_B G_0(\mathbf{k}) P_A G_0(\mathbf{k} + \mathbf{Q}) P_B \right], \quad (\text{S24})$$

- β_1 : Using the identities $\text{Tr}_{\sigma}[(\mathbf{N}_1 \cdot \boldsymbol{\sigma})^4] = 2|\mathbf{N}_1|^4$ and $\text{Tr}_{\sigma}[(\mathbf{N}_1 \cdot \boldsymbol{\sigma})(\mathbf{N}_1 \cdot \boldsymbol{\sigma})(\mathbf{N}_2 \cdot \boldsymbol{\sigma})(\mathbf{N}_2 \cdot \boldsymbol{\sigma})] = 2|\mathbf{N}_1|^2|\mathbf{N}_2|^2$, we derive:

$$\beta_1 = \frac{\lambda^4}{2\beta} \sum_n \sum_k \text{Tr} \left[G_0(\mathbf{k}) P_A G_0(\mathbf{k} + \mathbf{Q}) P_A G_0(\mathbf{k}) P_B G_0(\mathbf{k} + \mathbf{Q}) P_B \right]. \quad (\text{S25})$$

Finally, the validity of these analytically derived coefficients is confirmed by comparing the resulting free energy with the numerical results of the original trilayer Hamiltonian, as shown in Fig. S3. Fig. S3(a) demonstrates that the effective spin model (green line) accurately reproduces the angular dependence of the total energy obtained from the microscopic model (blue circles). Furthermore, Fig. S3(b) shows that the analytically derived biquadratic coefficient β_2 converges to the numerical result in the strong coupling limit, justifying the perturbative approach employed in this derivation.

1. Analytical calculation of coefficient β_2

In Eq. (S24), we have derived the expression of β_2 as,

$$\beta_2 = \frac{\lambda^4}{4\beta} \sum_n \sum_k \text{Tr} \left[G_0(\mathbf{k}) P_A G_0(\mathbf{k} + \mathbf{Q}) P_B G_0(\mathbf{k}) P_A G_0(\mathbf{k} + \mathbf{Q}) P_B \right] \quad (\text{S26})$$

From the expression of the bare Green function $G_0^{-1}(\mathbf{k}, i\omega_n) = (-i\omega_n - \mu) I_2 + \varepsilon_{\mathbf{k}} \tau_x$, we can rewrite it as

$$G_0(\mathbf{k}, i\omega_n) = \frac{(-i\omega_n - \mu) I_2 + \varepsilon_{\mathbf{k}} \tau_x}{(i\omega_n + \mu)^2 - \varepsilon_{\mathbf{k}}^2}. \quad (\text{S27})$$

By plugging in the expression of the Green function explicitly, we get the simplified expression of β_2 as,

$$\beta_2 = \frac{\lambda^4}{4\beta} \sum_n \sum_{\mathbf{k}} \frac{\varepsilon_{\mathbf{k}}^2 \varepsilon_{\mathbf{k} + \mathbf{Q}}^2}{[(i\omega_n + \mu)^2 - \varepsilon_{\mathbf{k}}^2]^2 [(i\omega_n + \mu)^2 - \varepsilon_{\mathbf{k} + \mathbf{Q}}^2]^2}. \quad (\text{S28})$$

Performing the Matsubara-frequency sum, we obtain the decomposition below, where the prefactors $A^{(\mathbf{k}, \mathbf{k} + \mathbf{Q})}(\mathbf{k})$ and $B^{(\mathbf{k}, \mathbf{k} + \mathbf{Q})}(\mathbf{k})$ are defined including the overall factor $\lambda^4/4$.

$$\beta_2 = \sum_k \left[A^{(\mathbf{k})}(\mathbf{k}) (n'_F(\varepsilon_{\mathbf{k}} - \mu) + n'_F(\varepsilon_{\mathbf{k}} + \mu)) - B^{(\mathbf{k})}(\mathbf{k}) (n_F(\varepsilon_{\mathbf{k}} - \mu) - n_F(-\varepsilon_{\mathbf{k}} - \mu)) \right] \quad (\text{S29})$$

$$+ A^{(\mathbf{k} + \mathbf{Q})}(\mathbf{k}) (n'_F(\varepsilon_{\mathbf{k} + \mathbf{Q}} - \mu) + n'_F(\varepsilon_{\mathbf{k} + \mathbf{Q}} + \mu)) - B^{(\mathbf{k} + \mathbf{Q})}(\mathbf{k}) (n_F(\varepsilon_{\mathbf{k} + \mathbf{Q}} - \mu) - n_F(-\varepsilon_{\mathbf{k} + \mathbf{Q}} - \mu)) \quad (\text{S30})$$

where

$$\begin{aligned} A^{(\mathbf{k})}(\mathbf{k}) &= \frac{\lambda^4 \varepsilon_{\mathbf{k} + \mathbf{Q}}^2}{16 \Delta_{\mathbf{k}}^2}, & A^{(\mathbf{k} + \mathbf{Q})}(\mathbf{k}) &= \frac{\lambda^4 \varepsilon_{\mathbf{k}}^2}{16 \Delta_{\mathbf{k}}^2}, \\ B^{(\mathbf{k})}(\mathbf{k}) &= \frac{\lambda^4 \varepsilon_{\mathbf{k} + \mathbf{Q}}^2}{16 \varepsilon_{\mathbf{k}} \Delta_{\mathbf{k}}^2} + \frac{\lambda^4 \varepsilon_{\mathbf{k}} \varepsilon_{\mathbf{k} + \mathbf{Q}}^2}{8 \Delta_{\mathbf{k}}^3}, & B^{(\mathbf{k} + \mathbf{Q})}(\mathbf{k}) &= \frac{\lambda^4 \varepsilon_{\mathbf{k}}^2}{16 \varepsilon_{\mathbf{k} + \mathbf{Q}} \Delta_{\mathbf{k}}^2} - \frac{\lambda^4 \varepsilon_{\mathbf{k} + \mathbf{Q}} \varepsilon_{\mathbf{k}}^2}{8 \Delta_{\mathbf{k}}^3} \end{aligned} \quad (\text{S31})$$

Here $\Delta_{\mathbf{k}} \equiv \varepsilon_{\mathbf{k}}^2 - \varepsilon_{\mathbf{k} + \mathbf{Q}}^2$. The first term, proportional to the derivative of the Fermi-Dirac distribution n'_F , represents the Fermi surface contribution. In contrast, the second term involving the n_F accounts for the Fermi sea contribution. This part integrates the energy redistribution across all occupied electronic states.

III. GEOMETRIC CANCELLATION OF THE BILINEAR EXCHANGE J_{eff}

In this section, we show that the bilinear term in Eq. (S20) for the commensurate stripe texture is geometrically canceled, i.e., $J_{\text{eff}} = 0$. The RKKY contribution between the two textures can be written as

$$\Delta \mathcal{F}_{12}^{(1)} = -\frac{1}{2} \sum_{\mathbf{r}, \mathbf{r}'} \chi(\mathbf{r} - \mathbf{r}') \mathbf{m}_T(\mathbf{r}) \cdot \mathbf{m}_B(\mathbf{r}' + \boldsymbol{\delta}), \quad (\text{S32})$$

$$= -\frac{1}{2} \sum_{\mathbf{q}} \chi(\mathbf{q}) \mathbf{m}_T(-\mathbf{q}) \cdot \left[e^{i\mathbf{q} \cdot \boldsymbol{\delta}} \mathbf{m}_B(\mathbf{q}) \right], \quad (\text{S33})$$

where χ is the static spin susceptibility of the middle-layer electrons. The phase factor $e^{i\mathbf{q} \cdot \boldsymbol{\delta}}$ arises solely from the fact that the two AFM layers are laterally shifted.

For the commensurate stripe texture, the only nonzero Fourier components are at $\mathbf{q} = \pm \mathbf{Q}$:

$$\mathbf{m}_T(\pm \mathbf{Q}) = \frac{\mathbf{N}_1}{2}, \quad \mathbf{m}_B(\pm \mathbf{Q}) = \frac{\mathbf{N}_2}{2}. \quad (\text{S34})$$

Substituting into Eq. (S33) and using $\chi(\mathbf{Q}) = \chi(-\mathbf{Q})$, we obtain

$$\Delta \mathcal{F}_{12}^{(1)} = -\frac{\chi(\mathbf{Q})}{4} (\mathbf{N}_1 \cdot \mathbf{N}_2) \cos(\mathbf{Q} \cdot \boldsymbol{\delta}). \quad (\text{S35})$$

Therefore $J_{\text{eff}} \propto \chi(\mathbf{Q}) \cos(\mathbf{Q} \cdot \boldsymbol{\delta})$. In our stacking, $\boldsymbol{\delta} = \hat{x}/2$ gives $\cos(\mathbf{Q} \cdot \boldsymbol{\delta}) = \cos(\pi/2) = 0$, hence $J_{\text{eff}} = 0$.

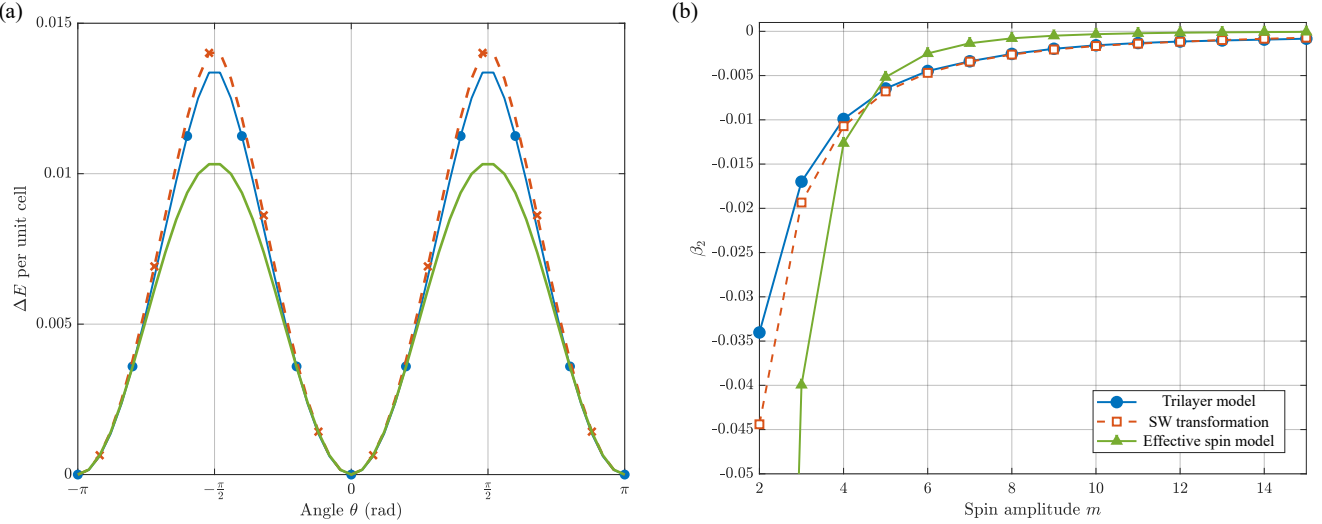


FIG. S3. (a) The relative total energy difference per unit cell as a function of the relative angle θ between the top and bottom layer magnetizations. The results from the microscopic Trilayer model in Eq. (S3) (blue) are compared with the effective Hamiltonian derived by SW transformation in Eq. (S8) (orange) and the effective spin model from Landau theory in Eq. (S20),(S21) (green). (b) The extracted biquadratic coupling coefficient β_2 as a function of the spin amplitude parameter m . The SW transformation (orange squares) and the effective spin model (green triangles) both converge to the exact Trilayer result (blue circles) in the large- m regime.

IV. SYMMETRY OF THE TIGHT-BINDING MODEL

In Eq. (S8), we have written the effective real-space Hamiltonian as,

$$\hat{H}_{\text{eff}} = -t_m \sum_{\langle i,j \rangle, \sigma} \left(c_{i,\sigma}^\dagger c_{j,\sigma} + \text{h.c.} \right) - \mu \sum_{i,\sigma} n_{i,\sigma} + \sum_{i \in A} c_i^\dagger [\mathbf{h}_A(\mathbf{r}_i) \cdot \boldsymbol{\sigma}] c_i + \sum_{j \in B} c_j^\dagger [\mathbf{h}_B(\mathbf{r}_j) \cdot \boldsymbol{\sigma}] c_j, \quad (\text{S36})$$

where the effective Zeeman fields are given as,

$$\mathbf{h}_A(\mathbf{r}_i) \equiv -\frac{t_\perp^2}{J|\mathbf{m}_T(\mathbf{r}_i)|^2} \mathbf{m}_T(\mathbf{r}_i), \quad \mathbf{h}_B(\mathbf{r}_j) \equiv -\frac{t_\perp^2}{J|\mathbf{m}_B(\mathbf{r}_j)|^2} \mathbf{m}_B(\mathbf{r}_j). \quad (\text{S37})$$

The commensurate stripe order is characterized by the wavevector $\mathbf{Q} = (\pi, 0)$, which breaks the primitive translational symmetry and doubles the unit cell. As a result, the Bloch Hamiltonian acts on an 8-dimensional internal space ($2 \times 2 \times 2$), arising from the sublattice, band-folding (due to unit-cell doubling), and spin degrees of freedom.

The total Bloch Hamiltonian is explicitly given by the sum of the kinetic and magnetic parts:

$$H(\mathbf{k}) = H_0(\mathbf{k}) + H_{\text{on}}(\theta). \quad (\text{S38})$$

$$\begin{aligned} H(k_x, k_y) = & t_m ((1 + \cos k_x)(\tau_x \otimes I_\rho \otimes I_\sigma) + (\sin k_x)(\tau_y \otimes I_\rho \otimes I_\sigma) \\ & + \frac{1}{2} [\cos(k_x - k_y) + \cos k_x + \cos k_y + 1] (\tau_x \otimes \rho_x \otimes I_\sigma) \\ & + \frac{1}{2} [\sin k_x + \sin(k_x - k_y) - \sin k_y] (\tau_y \otimes \rho_x \otimes I_\sigma) \\ & + \frac{1}{2} [-\sin(k_x - k_y) + \sin k_x + \sin k_y] (\tau_x \otimes \rho_y \otimes I_\sigma) \\ & + \frac{1}{2} [\cos(k_x - k_y) - \cos k_x + \cos k_y - 1] (\tau_y \otimes \rho_y \otimes I_\sigma) \\ & + H_{\text{on}}(\theta, h_A, h_B), \end{aligned} \quad (\text{S39})$$

where h_A and h_B denote the magnitudes of $\mathbf{h}_{A,B}(\mathbf{r})$, which are the induced exchange fields on the A and B sublattices. θ is defined as the relative angle between $\hat{\mathbf{h}}_A$ and $\hat{\mathbf{h}}_B$. Here, the Pauli matrices τ act on the sublattice (A/B) space,

encoding the layer-selective coupling. ρ act on the folded-band (backfolding) space associated with the doubled unit cell induced by the stripe order. Finally, σ represents the physical spin degree of freedom.

The first six terms describe the spin-independent hopping of amplitude t_m (set as the energy unit), and H_{on} represents the onsite Zeeman potentials exerted by the two AFM layers.

$$H_{\text{on}}(\theta) = \frac{\cos(\theta/2)}{2} \left[(h_A + h_B) I_\tau \otimes \rho_z + (h_B - h_A) \tau_z \otimes \rho_z \right] \otimes \sigma_x \\ + \frac{\sin(\theta/2)}{2} \left[(h_B - h_A) I_\tau \otimes \rho_z + (h_A + h_B) \tau_z \otimes \rho_z \right] \otimes \sigma_y. \quad (\text{S40})$$

For $h_A = h_B \equiv h$, Eq. (S40) simplifies to

$$H_{\text{on}}(\theta) = h \left[\cos \frac{\theta}{2} (I_\tau \otimes \rho_z \otimes \sigma_x) + \sin \frac{\theta}{2} (\tau_z \otimes \rho_z \otimes \sigma_y) \right]. \quad (\text{S41})$$

Our model hosts several spatial and magnetic symmetries that constrain the electronic band degeneracies in momentum space. Table S1 summarizes these operations and their corresponding high-symmetry points. The detailed symmetry analysis and its physical consequences are described below.

A. Symmetry constraint on spin polarization of odd-parity magnetism

We first summarize the relevant spin-space symmetries and the resulting constraints on spin polarization in an odd-parity magnetic state. For a spin- $\frac{1}{2}$ degree of freedom, a π -rotation about the z axis is represented by

$$C_{2z}^S = e^{-i\frac{\pi}{2}\sigma_z} = -i\sigma_z, \quad (\text{S42})$$

and acts on Pauli matrices via conjugation:

$$C_{2z}^S \sigma_x (C_{2z}^S)^{-1} = -\sigma_x, \quad C_{2z}^S \sigma_y (C_{2z}^S)^{-1} = -\sigma_y, \quad C_{2z}^S \sigma_z (C_{2z}^S)^{-1} = +\sigma_z. \quad (\text{S43})$$

Next, we define the combined unitary operator

$$\mathcal{S} \equiv T_{(1,1)} C_{2z}^S, \quad (\text{S44})$$

where $T_{(1,1)}$ is a lattice half-translation operator by a vector $\mathbf{T} = \frac{1}{2}\mathbf{a}_2 = (1, 1)$. In the $2 \times 2 \times 2$ basis, $T_{(1,1)}$ is defined as

$$T_{(1,1)} = I_\tau \otimes \begin{pmatrix} 0 & e^{ik_y/2} \\ e^{-ik_y/2} & 0 \end{pmatrix} \otimes I_\sigma. \quad (\text{S45})$$

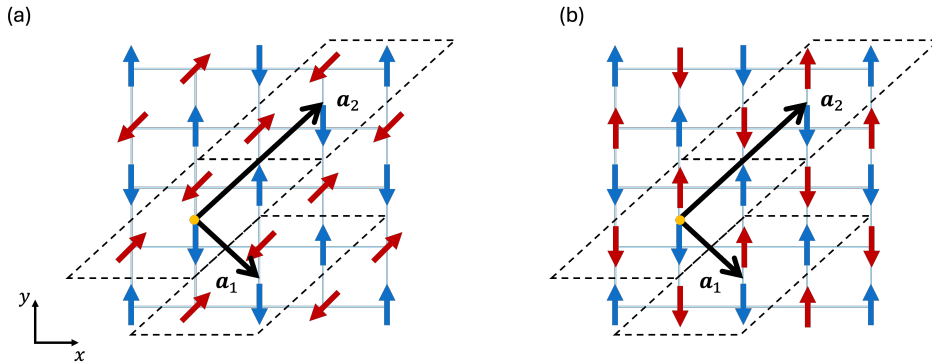


FIG. S4. Lattice structure of the trilayer model projected into 2D. (a) and (b) each represents the case when the angle between the Néel vectors of two layers is $\pi/4$ and 0 respectively. Dashed parallelogram marks the unit cell and black arrows represent the lattice vectors $\mathbf{a}_1 = a(1, -1)$ and $\mathbf{a}_2 = a(2, 2)$, where a is a lattice constant. The yellow dot marks the center of the unit cell.

Since $T_{(1,1)}$ only acts on orbital/sublattice space and C_{2z}^S acts on spin space, one has

$$\mathcal{S} \sigma_{x,y} \mathcal{S}^{-1} = -\sigma_{x,y}, \quad \mathcal{S} \sigma_z \mathcal{S}^{-1} = \sigma_z. \quad (\text{S46})$$

We also define the antiunitary operator

$$\Xi \equiv T_{(1,1)} \mathcal{T}, \quad (\text{S47})$$

where $\mathcal{T} = i\sigma_y \mathcal{K}$ is the time-reversal operator satisfying $\mathcal{T}^2 = -1$, with \mathcal{K} denoting complex conjugation. It flips the spin:

$$\mathcal{T} \boldsymbol{\sigma} \mathcal{T}^{-1} = -\boldsymbol{\sigma}. \quad (\text{S48})$$

Let $H(\mathbf{k})$ be the Bloch Hamiltonian. Since the half-translation $T_{(1,1)}$ maps the lattice into the spin-flipped configuration and the spin operations C_{2z}^S and \mathcal{T} flip it back, one can derive the following relations:

$$\mathcal{S}(\mathbf{k}) H(\mathbf{k}) \mathcal{S}(\mathbf{k})^{-1} = H(\mathbf{k}), \quad (\text{S49})$$

$$\Xi(\mathbf{k}) H(\mathbf{k}) \Xi(\mathbf{k})^{-1} = H(-\mathbf{k}). \quad (\text{S50})$$

We now show that the spin polarization is symmetry-enforced to be collinear along the z direction as a consequence of Eq. (S49).

Let $|u_{n\mathbf{k}}\rangle$ be the eigenstate of the Bloch Hamiltonian $H(\mathbf{k})$ satisfying $H(\mathbf{k})|u_{n\mathbf{k}}\rangle = E_n(\mathbf{k})|u_{n\mathbf{k}}\rangle$ and $\mathcal{S}(\mathbf{k})|u_{n\mathbf{k}}\rangle = \lambda_{n\mathbf{k}}|u_{n\mathbf{k}}\rangle$. Then

$$\langle \sigma_x \rangle_{n\mathbf{k}} = \langle u_{n\mathbf{k}} | \sigma_x | u_{n\mathbf{k}} \rangle = \langle u_{n\mathbf{k}} | (\mathcal{S} \sigma_x \mathcal{S}^{-1}) | u_{n\mathbf{k}} \rangle = -\langle \sigma_x \rangle_{n\mathbf{k}}, \quad (\text{S51})$$

so $\langle \sigma_x \rangle_{n\mathbf{k}} = 0$, and similarly $\langle \sigma_y \rangle_{n\mathbf{k}} = 0$. Thus,

$$\langle \sigma_x \rangle_{n\mathbf{k}} = 0, \quad \langle \sigma_y \rangle_{n\mathbf{k}} = 0, \quad \langle \sigma_z \rangle_{n\mathbf{k}} \text{ can be nonzero.} \quad (\text{S52})$$

Moreover, the antiunitary symmetry Ξ enforces oddness of the spin polarization under $\mathbf{k} \rightarrow -\mathbf{k}$. From Eq. (S50), the state $\Xi|u_{n\mathbf{k}}\rangle$ is an eigenstate at $-\mathbf{k}$ with the same energy, $E_n(-\mathbf{k}) = E_n(\mathbf{k})$. For the spin expectation value $\mathbf{s}_n(\mathbf{k}) \equiv \langle u_{n\mathbf{k}} | \boldsymbol{\sigma} | u_{n\mathbf{k}} \rangle$, define $|u_{n,-\mathbf{k}}\rangle = \Xi|u_{n\mathbf{k}}\rangle$. Then

$$\mathbf{s}_n(-\mathbf{k}) = \langle u_{n\mathbf{k}} | \Xi^{-1} \boldsymbol{\sigma} \Xi | u_{n\mathbf{k}} \rangle = -\mathbf{s}_n(\mathbf{k}). \quad (\text{S53})$$

Finally, consistent with the underlying lattice geometry that hosts the translation $T_{(1,1)}$, the Hamiltonian also respects a mirror-reflection symmetry $M_{y=x}$ along the diagonal \mathbf{a}_2 . In matrix representation, $M_{y=x}$ reads

$$M_{y=x} = \begin{pmatrix} 1 & 0 \\ 0 & e^{ik_x} \end{pmatrix} \otimes I_\rho \otimes I_\sigma, \quad (\text{S54})$$

satisfying the following relations:

$$M_{y=x} H(k_x, k_y) M_{y=x}^{-1} = H(-k_x, k_y), \quad M_{y=x} \boldsymbol{\sigma} M_{y=x}^{-1} = \boldsymbol{\sigma}. \quad (\text{S55})$$

Then the same argument as above gives

$$s_z(-k_x, k_y) = s_z(k_x, k_y). \quad (\text{S56})$$

Combining Eq. (S56) with Eq. (S53) yields $s_z(k_x, -k_y) = -s_z(k_x, k_y)$.

Therefore, a structure respecting the symmetry \mathcal{S} exhibits an odd-parity spin splitting with spin polarization constrained to the z direction.

B. Kramers degeneracy on Γ -X

The system preserves an antiunitary symmetry $\tilde{\Theta}$ constructed as a composite operation of time-reversal \mathcal{T} , a mirror reflection $M_{y=x}$, and a half-lattice translation $T_{(1,1)}$:

$$\tilde{\Theta} = M_{y=x} T_{(1,1)} \mathcal{T}.$$

The explicit matrix representation of $\tilde{\Theta}$ is given by:

$$\tilde{\Theta}(k_x, k_y) = \left(\frac{1 + e^{ik_x}}{2} I_\tau + \frac{1 - e^{ik_x}}{2} \tau_z \right) \otimes \left(\frac{1 + e^{ik_y/2}}{2} \rho_x + \frac{1 - e^{ik_y/2}}{2i} \rho_y \right) \otimes (i \sigma_y \mathcal{K}),$$

satisfying $\tilde{\Theta} H(k_x, k_y) \tilde{\Theta}^{-1} = H(k_x, -k_y)$. The square of the antiunitary operator $\tilde{\Theta}$ satisfies $\tilde{\Theta}^2 = -e^{ik_y} I_{\tau\rho\sigma}$. Therefore, specifically along the Γ -X line ($k_y = 0$), the relation $\tilde{\Theta}^2 = -I$ holds. By Kramers' theorem, this symmetry enforces a line double degeneracy throughout the Γ -X path, which remains protected regardless of the magnetic parameters (h_A, h_B, θ) .

C. Kramers degeneracy on X-M

Along the high-symmetry X-M line ($k_x = \pi$), the momentum-dependent hopping terms vanish, simplifying the Hamiltonian to depend only on the onsite potentials. In the symmetric limit where the two AFM layers are equivalent ($h_A = h_B$), the Hamiltonian $H(\pi, k_y)$ preserves an additional unitary symmetry U :

$$U = \tau_x \otimes I_\rho \otimes \sigma_x.$$

This operator commutes with the Hamiltonian ($[H, U] = 0$) for all k_y along this path.

The degeneracy arises from the interplay between this unitary symmetry U and the global antiunitary symmetry $\tilde{\Theta}$. Crucially, since U acts on spin as σ_x while $\tilde{\Theta}$ involves $i\sigma_y \mathcal{K}$, the two symmetries satisfy an anticommutation relation:

$$\{\tilde{\Theta}, U\} = 0.$$

This algebraic constraint dictates that every energy eigenstate along the X-M line must form a four-dimensional irreducible representation. Physically, the anticommutation ensures that $\tilde{\Theta}$ maps an eigenstate $|\psi\rangle$ from the $U|\psi\rangle = |\psi\rangle$ sector to a degenerate Kramers partner in the $U|\psi\rangle = -|\psi\rangle$ sector. Consequently, all bands exhibit a robust four-fold degeneracy along the X-M line. This symmetry protection explains the characteristic band sticking observed in Fig. 2 of the main text, which is lifted immediately upon deviating from $k_x = \pi$ or breaking the layer equivalence ($h_A \neq h_B$).

D. Non-symmorphic symmetry \mathcal{U}_{ns} at $\theta = \pi/2$

In the orthogonal limit ($\theta = \pi/2$), the system restores a specific nonsymmorphic symmetry generated by the composite operator \mathcal{U}_{ns} . This operator combines a lattice translation $\mathbf{T} = a(1, 0)$ with a 90° spin-rotation about the z-axis:

$$\mathcal{U}_{\text{ns}} \equiv T_{(1,0)} C_{4z}^S, \quad C_{4z}^S = e^{-i(\pi/4)\sigma_z}.$$

Along this line, the operator \mathcal{U}_{ns} commutes with the Bloch Hamiltonian ($[\hat{H}, \mathcal{U}_{\text{ns}}] = 0$). Consequently, the energy bands can be block-diagonalized into distinct sectors labeled by the eigenvalues of \mathcal{U}_{ns} . Since hybridization between eigenstates belonging to different sectors is strictly forbidden, any band crossings occurring between them are symmetry-protected. These robust crossings constitute the Dirac nodal line discussed in the main text, which remains gapless against any perturbation that preserves \mathcal{U}_{ns} .

TABLE S1. Symmetry operations of the trilayer model.

Label	Operator G	symmetry preserving angle	invariant momenta	degeneracy
$\tilde{\Theta}$	$M_{y=x} T_{(1,1)} \mathcal{T}$	$\theta \in [0, 2\pi)$	full BZ	Two-fold line
U	$\tau_x \otimes I_\rho \otimes \sigma_x$	$\theta \in [0, 2\pi)$	X-M line	Four-fold line
\mathcal{U}_{ns}	$T_{(1,0)} C_{4z}^S$	$\theta = \pi/2$	full BZ	Two-fold nodal line
\mathcal{PT}	$\tau_x \otimes \rho_x \otimes i\sigma_y \mathcal{K}$	$\theta = 0$	full BZ	Two-fold degeneracy

E. \mathcal{PT} -symmetry at $\theta = 0$

In the collinear limit ($\theta = 0$), the effective Hamiltonian restores a global antiunitary \mathcal{PT} -symmetry. This symmetry combines time-reversal with spatial inversion. The explicit operator representation is given as,

$$\mathcal{PT} = \tau_x \otimes \rho_x \otimes i\sigma_y \mathcal{K}. \quad (\text{S57})$$

This anti-unitary operator satisfies $(\mathcal{PT})^2 = -I_{\tau\rho\sigma}$, enforcing a twofold degeneracy throughout the Brillouin zone.